Arabian Journal of Chemistry (2020) **13**, 8372–8387

King Saud University

Arabian Journal of Chemistry

www.ksu.edu.sa
www.sciencedirect.com

ORIGINAL ARTICLE

Near infrared-driven photoelectrochemical water splitting: Review and future prospects

Ping-Yen Hsieh [a], **Jhen-Yang Wu** [a], **Tso-Fu Mark Chang** [b,*], **Chun-Yi Chen** [b,*], **Masato Sone** [b], **Yung-Jung Hsu** [a,c,*]

[a] *Department of Materials Science and Engineering, National Chiao Tung University, Hsinchu 30010, Taiwan*
[b] *Institute of Innovative Research, Tokyo Institute of Technology, 4259 Nagatsuta-cho, Midori-ku, Yokohama 226-8503, Japan*
[c] *Center for Emergent Functional Matter Science, National Chiao Tung University, Hsinchu 30010, Taiwan*

Received 2 April 2020; accepted 18 May 2020
Available online 29 May 2020

KEYWORDS

PEC water splitting;
Near infrared-driven;
Solar hydrogen production

Abstract Photoelectrochemical (PEC) water splitting supplies an environmentally friendly, sustainable approach to generating renewable hydrogen fuels. Oxides semiconductors, e.g. TiO_2, $BiVO_4$, and Fe_2O_3, have been widely developed as photoelectrodes to demonstrate the utility in PEC systems. Even though significant effort has been made to increase the PEC efficiency, these materials are still far from practical applications. The main issue of metal oxides is the wide bandgap energy that hinders effective photons harvesting from sunlight. In solar spectrum, over 40% of the energy is located in the near-infrared (NIR) region. Developing sophisticated PEC systems that can be driven by NIR illumination is therefore essential. This review gives a concise overview on PEC systems based on the use of NIR-driven photoelectrodes. Promising candidates as efficient yet practical NIR-responsive photoelectrodes are suggested and discussed. Future outlooks on the advancement of PEC water splitting are also proposed.

1. Introduction

As the population and economy continue to surge, global demand for energy is increasing rapidly. Among energy sources, solar power is considered a promising alternative energy source due to its endless and considerable supply. In one year, solar energy can provide approximately 173,000 TW (Archer, 2011), which is around 9,600 times higher than the value of annual world energy consumption (18.39 TW in 2018 (Full Report, 2019). There exist many techniques to utilize solar energy, such as solar thermal power plants, solar cells, and solar fuels. Photoelectrochemical (PEC) water splitting provides an ideal method to obtain clean chemical fuels from the periodic solar power (Grätzel, 2001; Walter et al., 2010; Sivula and Krol., 2016). Water splitting produces hydrogen and oxygen, which are stable and harmless. Furthermore, hydrogen possesses a larger energy density (141.9 MJ/kg) than conventional fossil fuels (55.5 MJ/kg for methane; 47.5 MJ/kg

---

[*] Corresponding authors.
E-mail addresses: chang.m.aa@m.titech.ac.jp (T.-F.M Chang), chen.c.ac@m.titech.ac.jp (C.-Y. Chen), yhsu@cc.nctu.edu.tw (Y.-J. Hsu).

Peer review under responsibility of King Saud University.

Production and hosting by Elsevier

https://doi.org/10.1016/j.arabjc.2020.05.025

for gasoline; 20.0 MJ/kg for methaneol) (Kim et al., 2019a), making the PEC technique an appealing approach to meeting the global energy demand. Typical PEC systems comprise a working electrode (WE) along with a counter electrode (CE) immersed in specific eleectrolyte. In a typical configuration, semiconductors with photoactivity are selected as the WE, and Pt wire acts as the CE. Fig. 1 depicts the fundamental of PEC water splitting by using semiconductors as photoelectrodes. For an n-type semiconductor, light irradiation with energy larger than its bandgap (E_g) generates electron-hole pairs. These charge carriers then diffuse to the electrode surface for participation in the subsequent redox reactions. The chemical potential equilibrium between n-type semiconductor and electrolyte creates an upward band bending at interface. Under anodic bias condition, the photoexcited holes drift along the bent band to inject into the electrolyte, oxidizing water to produce oxygen; meanwhile, the photogenerated electrons transfer through the external circuit to the CE, reducing water to produce hydrogen. In this configuration, n-type semiconductor functions as photoanode since water oxidation takes place at the electrode surface. For p-type semiconductors, photoexcited charge carriers transfer in an opposite direction as a consequence of downward band bending at interface, evincing electron injection into electrolyte and hole transportation to the CE. Under this scenario, water reduction occurs at the semiconductor surface for producing hydrogen, while water oxidation takes place at CE to generate oxygen. Therefore, p-type semiconductor acts as photocathode in a PEC cell.

It should be noted that the photoexcited charge carriers are inclined to charge recombination when they diffuse from the bulk of the semiconductor to the surface. Only a fraction of the charge carriers can be extracted and contribute to water splitting reactions. The measured photocurrent density (J_{pec}) serves as a global index to evaluate the carrier utilization efficiency in PEC water splitting. The recorded J_{pec} equates the product of theoretical photocurrent density (J_{abs}), charge separation efficiency at bulk (η_{sep}), and carrier injection efficiency at surface (η_{inj}). The following equation shows the relationship among these values: $J_{pec} = J_{abs} \times \eta_{sep} \times \eta_{inj}$. Here, J_{abs} denotes the maximum photocurrent attained by presuming all of the harvested photons are converted into electrons; η_{sep} represents percentage of charge carriers produced at bulk that can eventually reach to the semiconductor surface; η_{inj} stands for percentage of charge carriers reaching to surface that are ultimately injected into the electrolyte. Empirically, J_{abs} can be calculated by measuring the photons harvesting efficiency and integrating it over the AM 1.5G spectrum. On the other hand, when J_{pec} is measured in an electrolyte containing charge carrier scavenger (e.g. sulphite for photoanode, peroxide for photocathode), the kinetics loss of charge injection can be neglected and η_{inj} is assumed to be 100%. The value of η_{sep} can then be obtained by dividing J_{pec} (measured in the presence of scavenger) by J_{abs}. The actual η_{inj} can be further calculated by dividing J_{pec} measured in a regular electrolyte by J_{abs} and η_{sep} (Lee et al., 2019a). It is noteworthy that the band structure of semiconductors determines whether or not water splitting reaction can occur. The chemical potential of water reduction and oxidation is respectively located at 0 and 1.23 V vs. reversible hydrogen electrode (RHE). In order for water splitting to spontaneously occur, the conduction band minimum (CBM) and valence band maximum (VBM) of selected semiconductors must straddle 0 and 1.23 V vs. RHE such that sufficient thermodynamic driving force can be supplied. However, an overpotential of approximately 0.5 eV is needed to conquer the kinetic barrier of surface reactions (Jiang et al., 2017). Therefore, the required bandgap of the semiconductor is at least 1.8 eV; otherwise, extra energy input is required to initiate the reactions. Aside from the typical single-photoelectrode PEC construction, a tandem cell composed of two photoelectrodes (PEC-PEC) or one photoelectrode and one photovoltaic cell (PV-PEC) has emerged as a new frontier in PEC water splitting. Such a tandem configuration can absorb incident light by two absorbers and operate under unbiased conditions, which holds promise of converting solar energy into chemical fuels in a sustainable manner.

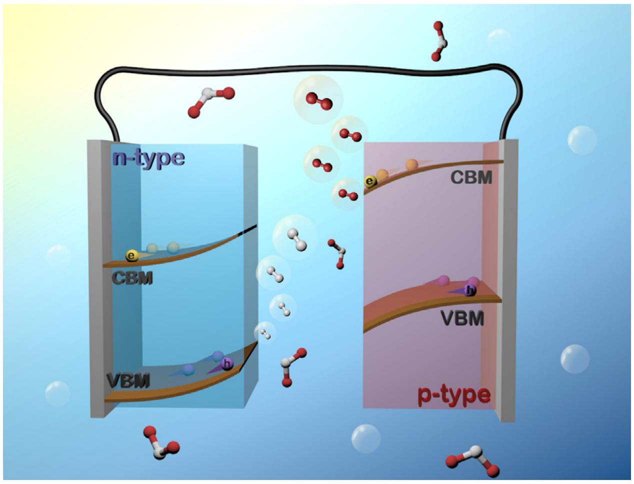

Fig. 1 Fundamental principle of employing semiconductor photoelectrodes to conduct PEC water splitting.

The bandgap energy of semiconductors provides a major parameter that affects the solar to hydrogen (STH) conversion efficiency. Note that solar spectrum comprises around 7% of energy in ultraviolet (UV) region ($\lambda < 400$ nm), 39% of energy in visible region ($400 < \lambda < 700$ nm), and 54% of energy in near-infrared (NIR) region ($700 < \lambda < 3000$ nm). Obviously, the NIR region constitutes most of the energy in sunlight. Non-toxic and highly stable TiO_2 is first demonstrated as photoelectrode to conduct water splitting. However, the large bandgap (~3.2 eV) prohibits TiO_2 from harvesting a large portion of sunlight (Do et al., 2020). Even though all the harvested photons are converted to electrons, the STH of TiO_2 is merely 1%. Some other metal oxides with medium bandgap, for example, $BiVO_4$ (Tayebi and Lee, 2019; Kim and Lee, 2019b), Fe_2O_3 (Shen et al., 2016; Sharma et al., 2019), Cu_2O (Pan et al., 2018; Bagal et al., 2019) have demonstrated remarkable visible light-driven photoactivity in PEC water splitting. A decent STH as high as 2.67% can be achieved by $BiVO_4$ photoanode (Ye et al, 2019). Despite the advances made so far, the solar energy utilization in these PEC systems is limited to UV and visible regions, and the achievable STH is still far from the requirement of industrial applications (STH = 30%). In the aim of further improving the PEC efficiency, exploitation of photoelectrodes to utilize NIR is highly desirable. In this review article, we first introduce the up-to-date development of NIR-driven PEC systems. After that, we propose several promising candidates as NIR-responsive photoelectrodes and photocatalysts, and provide insights into the future advancement of PEC water splitting.

2. NIR-driven photoelectrodes

The theoretical, maximum photocurrent that the semiconductor photoelectrodes can generate is when all the harvested photons are converted to electrons. In other words, the photons harvesting range of semiconductor directly determines the maximum STH value. Therefore, broadening the absorption wavelength as much as possible is a good strategy to enhance the PEC efficiency. Below, we introduce three promising materials categories for practical use as NIR-responsive photoelectrodes in PEC water splitting.

2.1. Chalcogenides

Chalcogenides semiconductors have sufficiently narrow bandgap energy that enables them to harvest photons from the NIR spectrum. Much effort has thus been made to exploit these ancient semiconductors for solar PEC water splitting. Earth-abundant nontoxic SnS has a small bandgap (1.4 to 1.7 eV), high absorption coefficient ($>10^4$ cm^{-1}), and intrinsic p-type semiconductor property, making it a hopeful photocathode candidate in PEC system. Various synthetic approaches have been devised to fabricate SnS photocathodes for PEC water splitting (Antunez et al., 2014; Seal et al., 2015; Gao et al., 2016; Shiga et al., 2016; Cheng et al., 2018). The measured photocurrents can reach 0.6 to 0.7 mA/cm^2 in an aqueous solution at pH 1. The PEC performance of SnS can be further improved with proper surface modification. In Patel's study (Patel et al., 2017), SnS films were synthesized by radio frequency magnetron sputtering and subject to a post-annealing treatment to enhance the PEC performance. In Fig. 2(a_1-a_4), the scanning electron microscopy (SEM) images displayed that SnS did not undergo significant morphological change upon thermal treatment at various temperatures. In Fig. 2(b-d), the photocurrent of the as-deposited SnS was approximately 2.0 mA/cm^2 at -0.2 V vs. RHE. The photocurrent density was enlarged to 5.6 mA/cm^2 upon heat treatment at 400 °C. Such a photoactivity enhancement originated from the reduced charge recombination at the SnS surface. The authors further conducted incident photon to current conversion efficiency (IPCE) analysis to observe the photoresponse wavelength of SnS. As revealed in Fig. 2(e), the modified SnS photocathodes exhibited photoactivity across UV, visible and NIR region. As cathodically enlarging the voltage from $+0.1$ to -0.3 V vs. RHE, the IPCE was enhanced by 14% under illumination at $\lambda < 420$ nm. This study demonstrated the promising potential of SnS as NIR-driven photocathode for solar water splitting.

With favourable properties including narrow bandgap energy (1.1–1.2 eV), large hole mobility (2.59 $cm^2/V/s$) and large absorption coefficient ($>10^5$ cm^{-1}), Sb_2Se_3 is also considered an appealing NIR-responsive photocathode for solar water splitting. Assuming 100% of IPCE, the theoretical photocurrent of Sb_2Se_3 can reach as high as 38 mA/cm^2. However, most of the previous studies on Sb_2Se_3 photocathodes failed to achieve the theoretical photocurrent (Prabhakar et al., 2017; Kim et al., 2017; Zhang et al., 2017; Yang et al., 2018; Park et al., 2019; Lee et al., 2019b; Yang and Moon, 2019). This failure was because of the lack of concurrent control over film thickness and crystallographic orientation, which induced optical and electrical losses to deteriorate PEC performance. In Park's work (Park et al., 2020), a bilayer Sb_2Se_3 nanostructure comprising vertical nanorods assembled on a compact monolayer was proposed to demonstrate the practical use of Sb_2Se_3 photocathodes. Fig. 3(a_1-a_2) shows the SEM images for the compact monolayer and bilayer structure of Sb_2Se_3. For bilayer structure, the optimal thickness of each layer was adjusted to 270 nm for bottom compact layer and 600 nm for nanorod layer. As shown in Fig. 3(b), the recorded photocurrent of bilayer Sb_2Se_3 reached 30 mA/cm^2 at 0 V vs. RHE in H_2SO_4 electrolyte, almost twice that of the monolayer structure. In Fig. 3(c), the bilayer structure exhibited 85% IPCE at 750 nm, and the photoactivity spanned the NIR region to 1000 nm. On the contrast, the IPCE of the monolayer was only 40% at 700 nm. The intensity-modulated photovoltage spectroscopic (IMVS) and electrochemical impedance spectroscopic (EIS) data confirmed that nanorod arrays enhanced charge dynamics as a consequence of the collective effects from increased surface area and favourable microstructural orientation. On the other hand, absorption spectra showed that bilayer Sb_2Se_3 had increased photons harvesting ability by virtue of the decreased light reflection and enhanced light scattering. The synergetic effect of efficient charge carrier and effective photon absorption contributed to the superior PEC performance observed for the bilayer structure. The findings of this work illustrated the promising potential of Sb_2Se_3 hierarchical nanostructures as NIR-driven photocathodes for practical use in PEC systems.

Two-dimensional (2-D), few-atoms-thick layers of transition metal dichalcogenides (TMDs), for example, MoS_2, WS_2 and $MoSe_2$ (Tekalgne et al., 2019a; Tekalgne et al., 2019b; Guo et al., 2019; Nguyen et al., 2018; Tekalgne et al, 2020a), and MXenes, which are composed of metal carbides and carbonitrides (Su et al., 2019; Nguyen et al, 2020a; Nguyen et al., 2020b; Hasani et al., 2019a), have drawn intense attentions for miscellaneous optoelectronics applications (Ma et al., 2018; Lee et al., 2019c; Atkin et al., 2016; Asunción-Nadal et al, 2020; Efekhari, 2017; Yu and Sivula, 2016; Jin et al., 2018; Tekalgne et al., 2020b; Hasani et al., 2019b; Nguyen et al., 2020c; Nguyen et al., 2020d). Particularly, the suitable bandgap and large absorption coefficient make TMDs (Hasani et al., 2019c) and MXenes (Nguyen et al., 2020e) ideal candidates for utilization in solar water splitting. Nevertheless, the highly variable concentration of defects resulting from the dangling bonds at the structure edge and the non-stoichiometry in the bulk has limited the practical use of these few-layer 2-D structures as photons harvesting materials. How to passivate the edge and internal defects of few-layer 2-D structures has thus been the key to advancing their utilization in solar energy conversion. In Yu's study (Yu et al., 2018), the practical use of WSe_2 nanoflakes as photocathodes for solar water splitting was realized with two passivation treatments to target the edge and internal defects. As depicted in Fig. 4 (a), pre-annealing (PA) treatment at 1100 °C and post surfactant treatment with hexyl-trichlorosilane (HTS) were performed to WSe2 nanoflakes in order to passivate the internal and edge defects. In this study, four exfoliated WSe_2 samples were prepared and compared, including one without any treatment (EX-AR), one with PA treatment only (EX-PA), one with HTS treatment only (EX-AR-HTS) and the other with

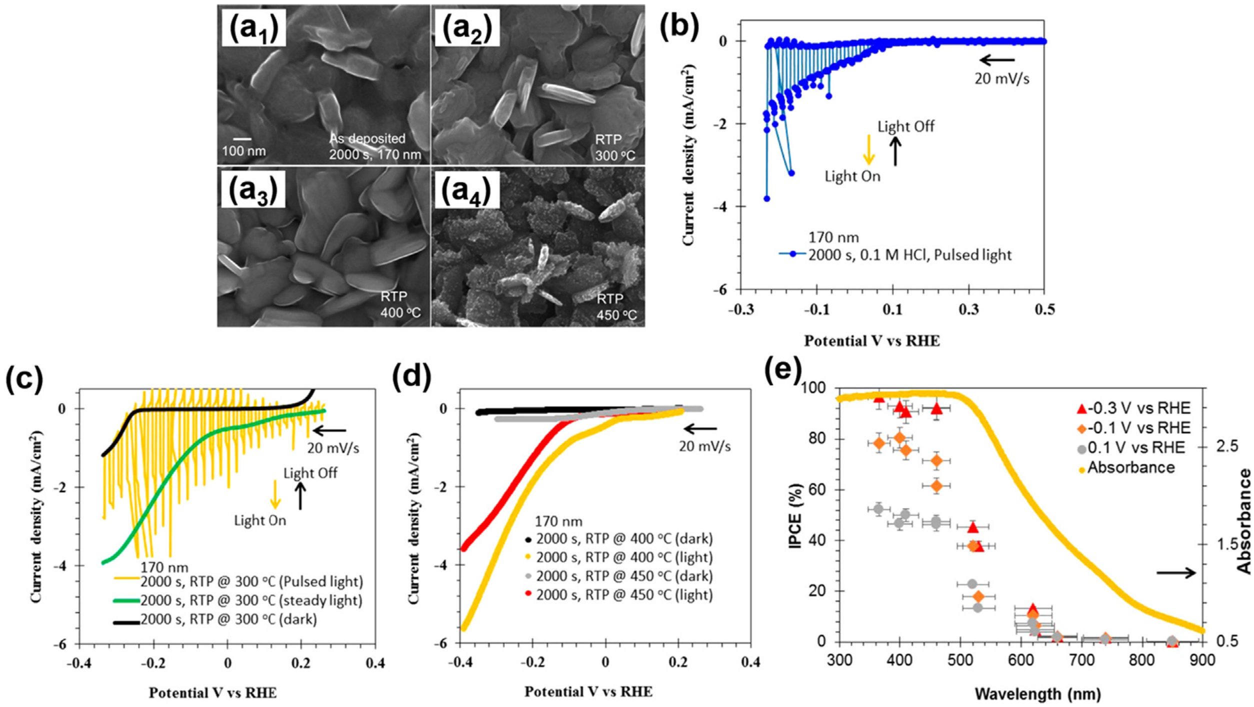

Fig. 2 SEM images of (a_1) as-deposited SnS and modified SnS at (a_2) 300 °C, (a_3) 400 °C, and (a_4) 450 °C. (b-d) I-V curves for as-deposited SnS and modified SnS. (e) IPCE data and the corresponding absorption spectrum for modified SnS under different applied potentials. Reprinted with permission (Patel et al., 2017). Copyright 2017, American Chemical Society.

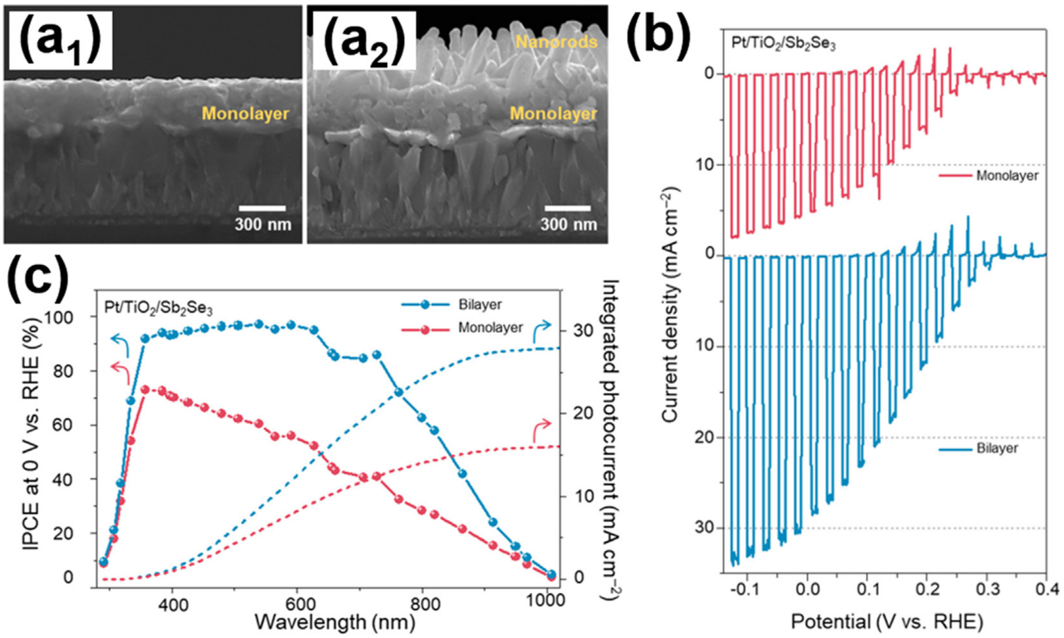

Fig. 3 SEM images of (a_1) compact monolayer, (a_2) bilayer structure of Sb_2Se_3. (b) I-t curves, (c) IPCE data and the integrated photocurrent values. Reprinted with permission (Park et al., 2020). Copyright 2020, American Chemical Society.

both PA and HTS treatments (EX-PA-HTS). Fig. 4(b_1-b_2) shows the typical TEM images for the samples before (Ex-AR) and upon PA treatment (Ex-PA). Similar lateral size was observed, implying that PA treatment did not affect the morphology of the exfoliated WSe_2. The samples were deposited with Pt-Cu co-catalyst for PEC measurements. In Fig. 4 (c), Ex-AR and Ex-PA displayed similar I-V curves, indicating that PA alone did not enhance the PEC activity of WSe_2. With HTS treatment, the two samples both showed enhanced photocurrents. Significantly, Ex-PA-HTS displayed much higher photocurrent than Ex-AR-HTS did, showing a benchmark photocurrent of 4.0 mA/cm^2 at 0 V vs. RHE. This outcome suggested that applying both PA and HTS treatments significantly enhanced the PEC activity of WSe_2. This photoactivity enhancement resulted from the passivation of internal and edge defects rendered by PA and HTS treatments. The IPCE data of Fig. 4 (d) further revealed that the photoactivity of Ex-PA-HTS spanned the whole visible to even NIR regions. The absorbed-photon-to-current efficiency (APCE) can reach 60% under illumination at 740 nm. These results highlighted the potential of the few-layered TMDs structures as efficient NIR-driven photocathodes for solar hydrogen production.

2.2. Chalcopyrites

As a prominent photoactive component in thin-film solar cells (Lopes et al., 2019; Chen et al., 2019; Birant et al., 2019; Ishizuka, 2019; Tseng et al., 2020), copper chalcopyrites have many intriguing properties suitable for converting solar energy. Key benefits include great photon to electron conversion efficiency and large absorption coefficient ($>10^4$ cm^{-1}) (Unold and Kaufmann, 2012), the two important features essential for PEC solar water splitting. Furthermore, the CBM of copper chalcopyrites is situated above the potential for water reduction, which enables them to function as photocathodes to conduct hydrogen production. Significantly, the bandgap of copper chalcopyrites can be readily tuned by controlling the composition, opening up new opportunities for extending the photoactivity to NIR region. Luo et al. proposed a solution-based method for preparation of $CuInS_2$ photocathodes by transforming the electrochemically deposited Cu_2O films in a solvothermal process (Luo et al., 2015). As shown in Fig. 5(a), the compact Cu_2O films were successfully transformed into porous $CuInS_2$ nanosheets with an enhanced density of active sites favourable for PEC reactions. However, the PEC performance of the as-obtained $CuInS_2$ was mediocre and instable, showing a considerably low saturated photocurrent of 100 $\mu A/cm^2$. This poor performance resulted from poor charge separation and slow reaction kinetics at the electrode/electrolyte interface. To address these issues, $CuInS_2$ was sequentially coated with CdS layer using chemical bath deposition, and bilayer of Al-doped ZnO (AZO) and TiO_2 using atomic layer deposition. Note that the CdS layer can form p-n junction with $CuInS_2$ to increase charge carrier separation, while the conformally deposited AZO and TiO_2 can function as protective layer to ensure chemical robustness. To facilitate surface reaction kinetics, Pt co-catalysts were further deposited. The modified $CuInS_2$ photocathodes attained a noticeable photocurrent density of 3.5 mA/cm^2 at −0.3 V vs. RHE, approximately 35 times increase over the as-obtained $CuInS_2$. As shown in Fig. 5(b), the photostability of the modified $CuInS_2$ was also enhanced, maintaining 80% of initial photocurrent after 2 hr of illumination. The IPCE data in Fig. 5 (c) further showed that the photoactivity of the modified $CuInS_2$ photocathodes can span across the UV to NIR region. This demonstration highlighted the promise of $CuInS_2$ as efficient NIR-driven photocathodes for durable operation in PEC water splitting.

Further bandgap engineering on $CuInS_2$ photocathodes by means of Ga addition can bring forth superior PEC properties including enhanced photocurrent and reduced onset potential. Septina et al. investigated the concentration effect of Ga addi-

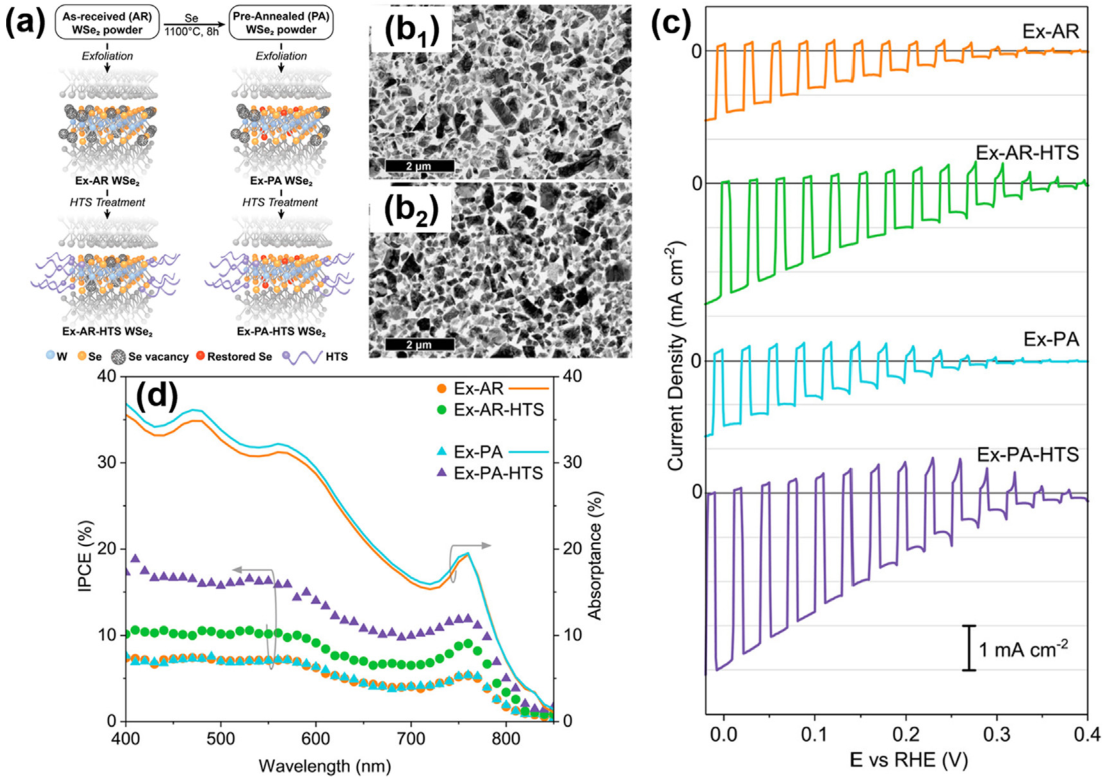

Fig. 4 (a) Scheme of WSe_2 preparation with PA and HTS treatments. TEM images for (b_1) Ex-AR and (b_2) Ex-PA WSe_2. (c) I-V curves and (d) IPCE data for the four samples. Reprinted with permission (Yu et al., 2018). Copyright 2018, American Chemical Society.

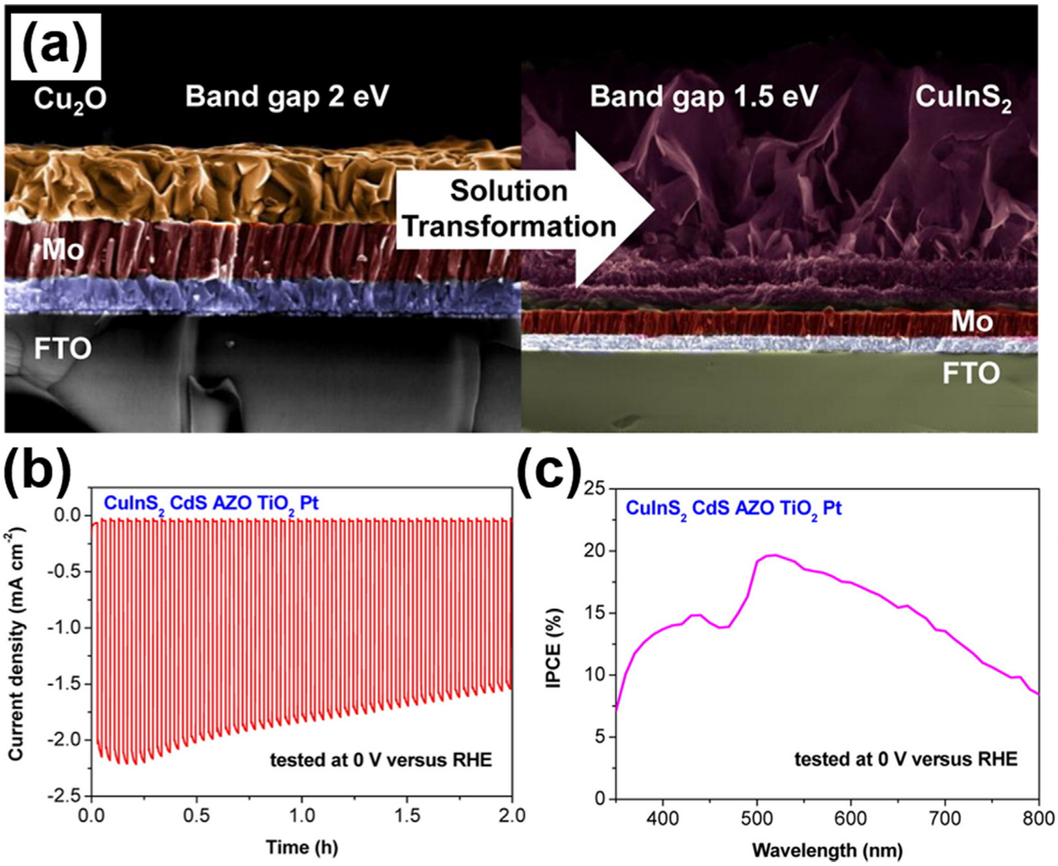

Fig. 5 (a) SEM images of the initial Cu_2O and the transformed $CuInS_2$. (b) I-t curves and (c) IPCE data for modified $CuInS_2$. Reprinted with permission (Luo et al., 2015). Copyright 2015, American Chemical Society.

tion on the PEC activity of $Cu(In,Ga)S_2$ (Septina et al., 2015). In this work, $Cu(In,Ga)S_2$ with various Ga amounts were prepared and the samples were labelled as CIGS(x), where x represented the ratio (%) of Ga/Ga + In. These samples were further modified with CdS deposition and Pt coating for use as photocathodes in PEC measurements. The relative band structure of CIGS(x) and CdS was constructed in Fig. 6(a) to better interpret the influence of Ga addition. Upon the addition of Ga, the bandgap of CIGS (x) expanded due to the transition of optical property from $CuInS_2$ to $GuGaS_2$. This property transition resulted in a slight increase of conduction band offset (CBO) and a great enlargement of interface bandgap (Eg_{int}). Note that these two parameters were important indexes to determine the carrier utilization efficiency for p-n junction. In particular, the enlarged Eg_{int} led to an increase in built-in potential at interface, which greatly enhanced photovoltage to reduce the overpotential of water reduction. As shown in Fig. 6 (b), among the different CIGS(x), CIGS(25) exhibited the highest photocurrent and the least cathodic onset potential. Although CIGS(40) had the largest Eg_{int}, the excessive Ga addition induced the formation of abundant midgap defects. These trap states would otherwise reduce the photovoltage to decrease the PEC performance. The IPCE data in Fig. 6(c) further revealed the vigorous photoactivity across the whole visible to NIR region for all the CIGS(x) samples.

2.3. *Plasmonic metals*

Noble metal nanostructures, e.g. Au, Ag and Cu, are capable of harvesting solar photons by virtue of the localized surface plasmon resonance (LSPR) property. LSPR states a peculiar optoelectronic feature resulting from the collective oscillation of conduction band electrons upon excitation of coherent incident light. The intensity and frequency of LSPR are highly related to chemical composition, and structural dimension and morphology of metal nanostructures. Such an intriguing feature has been extensively exploited in PEC applications (Hou and Cronin, 2013; Robatjazi et al., 2015). Significantly, the photoresponse of plasmonic metal nanostructures can be readily shifted to NIR region by means of compositional adjustment and morphological control. By functioning as antenna localizing the incident light, plasmonic metal nanostructures are capable of sensitizing semiconductors to incident photons with energy smaller than bandgap. Two near-field mechanisms, which include hot electron injection and plasmon resonance energy transfer, have been proposed to realize the LSPR-induced sensitizing effect. Since these two events are non-radiative processes, the resultant photoactivity enhancement is usually quite limited (<1%). Despite the limited enhancement, this approach offers an alternative route to the exploitation of NIR-driven photoelectrodes.

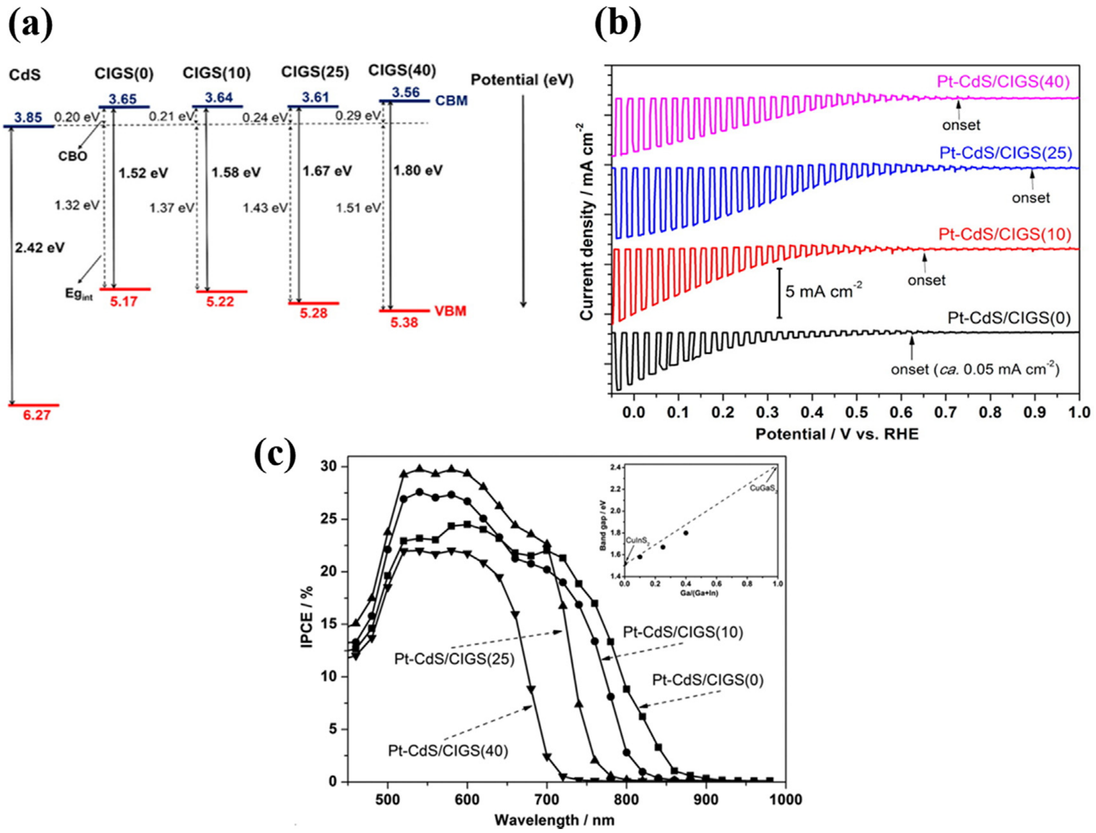

Fig. 6 (a) Relative band structure for CIGS(x) and CdS. (b) I-V curves and (c) IPCE data for Pt-CdS/CIGS(x). Reprinted with permission (Septina et al., 2015). Copyright 2015, American Chemical Society.

Employing TiO_2 as photoelectrodes in PEC systems has long been studied by virtue of the easy preparation, nontoxicity and stable chemical properties. However, TiO_2 is criticized for its large bandgap which only allows photons absorption in UV region. How to equip TiO_2 with visible and even NIR photoactivity has thus been in a limelight of research. In Pu's work (Pu et al., 2013), TiO_2 nanorods were deposited with Au nanoparticles (Au NP) and Au nanorods to demonstrate the extended photoactivity toward PEC water splitting. Note that Au NP and Au NR respectively displayed LSPR absorption around 550 and 720 nm. Introducing the two Au nanostructures can therefore extend the photoresponse of TiO_2 photoelectrodes to visible and even NIR region. Fig. 7(a_1-a_4) shows the TEM images for the successful deposition of Au NP and Au NR on TiO_2 nanorods. These Au nanostructures were firmly attached on TiO_2, which ensured effective near-field effect induced by LSPR excitation. The IPCE data of Fig. 7(b) clearly revealed the extended photoactivity for the two decorated TiO_2 photoelectrodes. The recorded IPCE peaks were well matched to the corresponding LSPR absorption peak. Significantly, further deposition of a mixture of Au NP and Au NR led to the photoresponse extension covering the whole visible to NIR region. As shown in Fig. 7(c), the Au NP-NR-deposited TiO_2 photoelectrodes displayed evenly enhanced IPCE covering both visible and NIR regions. This demonstration suggested that the LSPR-induced photoresponse of TiO_2 can be tuned by adjusting the structural morphology on the deposited Au.

It is important to note that the LSPR-induced photoactivity of plasmonic metal–semiconductor systems can be further augmented by exploiting the whispering gallery mode (WGM) resonance of the dielectric semiconductor component. The WGM resonance describes a type of light-mater interactions, which confines incident light around the circular ring boundary of a microcavity by total internal reflection. Numerical calculations suggest that the electric field of WGM can be strongly confined within the microcavity (Yang et al., 2015, providing foundation for further promoting the LSPR effect of the neighbouring plasmonic metals. Zhang's study demonstrated that the LSPR-enhanced activity of Au-decorated TiO_2 strongly depended on structural size of TiO_2, which can be realized by the prevalence of WGM resonance for large-sized TiO_2 (Zhang et al., 2016). Here, the function of WGM is to enhance and extend the LSPR absorption as well as magnify the interfacial electric field. These features can lead to a remarkable enhancement in PEC photoactivity. Finite element method (FEM) simulations suggested several important features of WGM resonance. First, small TiO_2 particles with the size of 60 nm did not express WGM in the visible region, therefore posing negligible effect on the LSPR absorption of Au. Second, the LSPR absorption of Au can be largely enhanced by the WGM resonance for large TiO_2 with 200–600 nm in size. Such an augmented LSPR effect was proportional to the TiO_2 size and can be ascribed to the enhancement in localized electromagnetic field induced by WGM resonance. Third, the WGM resonance was mostly localized underneath the TiO_2 surface, providing much feasibility of exploiting

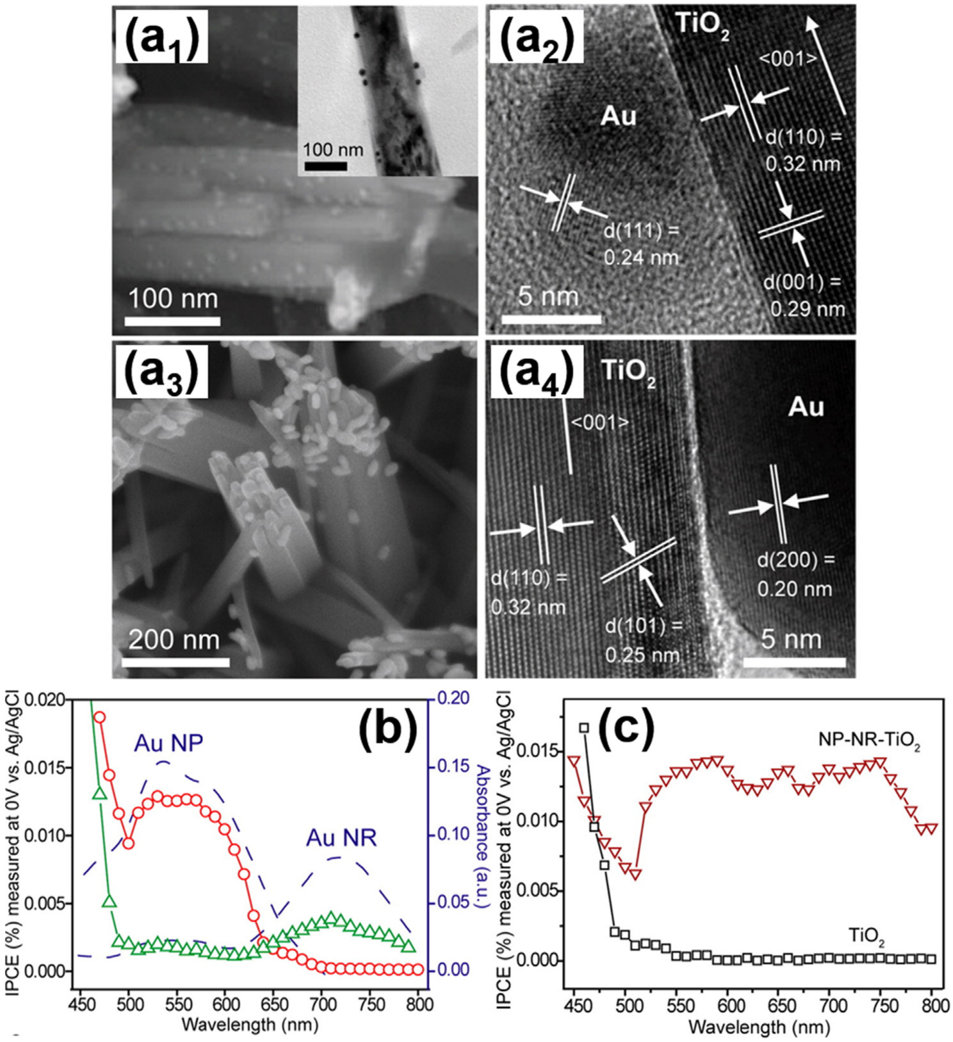

Fig. 7 SEM and TEM images for (a_1-a_2) Au NP-deposited TiO_2, (a_3-a_4) Au NR- deposited TiO_2. (b) IPCE data and the corresponding absorption spectra. (c) IPCE data for Au NP-NR-deposited TiO_2. Reprinted with permission (Pu et al., 2013). Copyright 2013, American Chemical Society.

WGM resonance by adjusting the relative location of Au. For example, when Au particles were partially encapsulated in large-sized TiO_2, the LSPR absorption was enhanced and red-shifted. By merely changing the size of TiO2 and the location of Au, both the LSPR intensity and frequency can be adjusted.

The simulation results can be further corroborated by experimental observations. Four relevant samples were prepared and compared, including pure TiO_2, isolated Au particle-decorated TiO_2 (Au mono-TiO_2), Au multimers-embedded TiO_2 (Janus Au multimer-TiO_2) and Au multimers-encapsulated TiO_2 (core@shell). Fig. 8(a_1-a_4) shows the corresponding TEM images. In Fig. 8(b), the absorption spectra clearly revealed the influence of Au location on the LSPR absorption of Au. Significantly, embedding Au multimers in TiO_2 can extend the LSPR wavelength toward NIR region, which was identified from the results of Janus Au multimer-TiO_2 and core@shell samples. These samples were further used as photocatalysts and photoelectrodes to conduct hydrogen production. In Fig. 8(c), the photocatalytic efficiency of hydrogen production upon visible-NIR illumination (λ > 420 nm) was compared. The activity of Au mono-TiO_2 (440 nm) was superior to the activity of Au mono-TiO_2 (60 nm). Importantly, Janus Au multimer-TiO_2 demonstrated the best photocatalytic efficiency. These results were consistent with the FEM simulations and confirmed that LSPR-enhanced photoactivity can be augmented by optimizing the size of TiO2 and the location of Au by means of WGM resonance. The superior photoactivity of Janus Au multimer-TiO_2 as photoelectrodes was further highlighted in the I-t curves and IPCE data shown in Fig. 8(d) and 8(e). Significantly, Janus Au multimer-TiO_2 exhibited photoactivity across the whole visible to NIR region. The findings from this work underlined that the synergy of WGM resonance and LSPR effect can provide a novel design principle for NIR-driven plasmonic photoelectrodes.

2.4. *Plasmonic semiconductors*

The LSPR can also occur on self-doped, nonstoichiometric semiconductors, such as MoO_{3-x} (Bai et al., 2015; Kasani et al., 2019; Odda et al., 2019), WO_{3-x} (Li et al., 2020a;

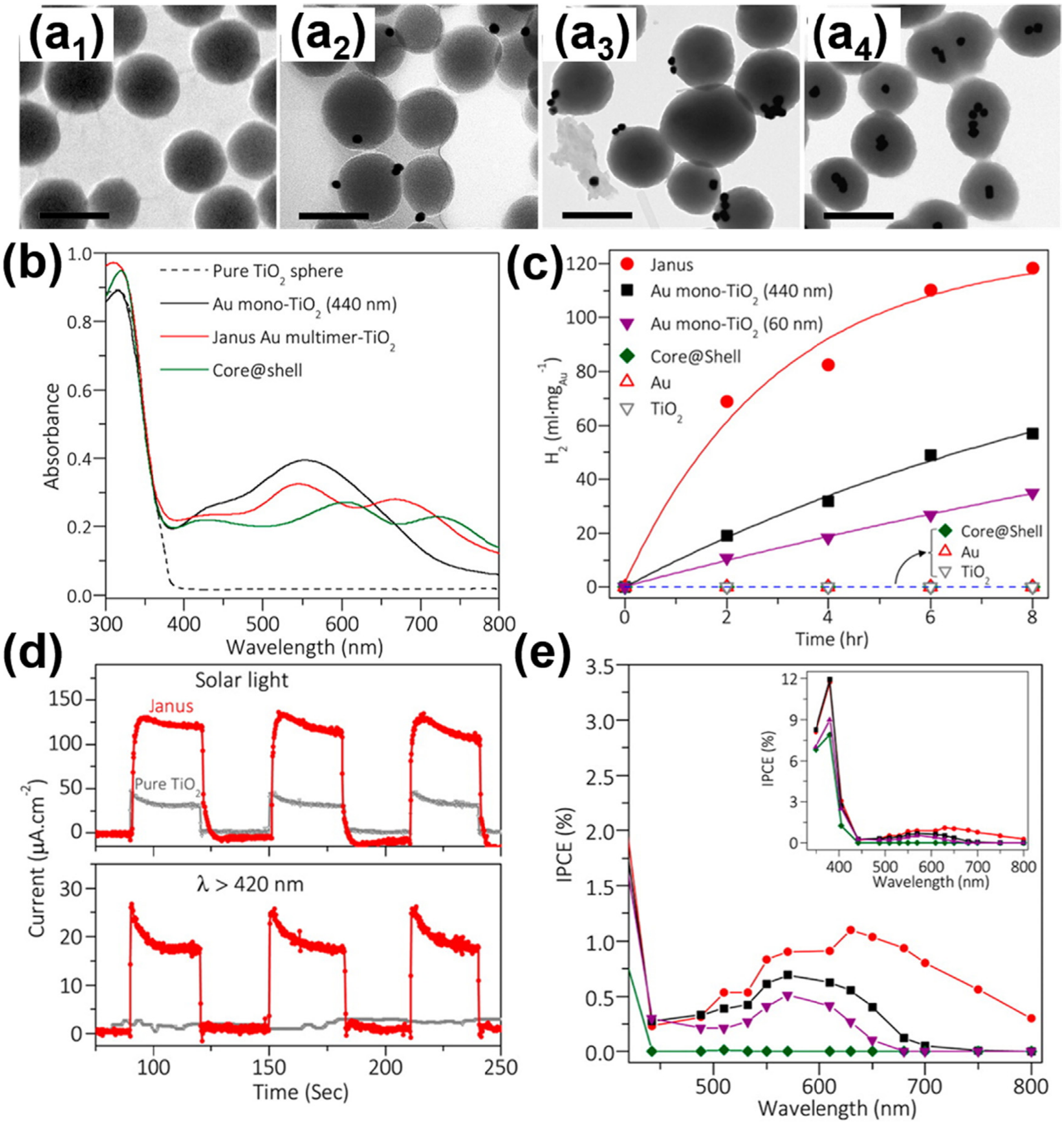

Fig. 8 TEM images (scale bar = 500 nm) for (a_1) pure TiO_2, (a_2) Au mono-TiO_2, (a_3) Janus Au multimer-TiO2, (a_4) core@shell. (b) Absorption spectra, (c) photocatalytic hydrogen production data, (d) I-t curves, (e) IPCE data for relevant samples. Reprinted with permission (Zhang et al., 2016). Copyright 2016, American Chemical Society.

Pan et al., 2017; Ren et al., 2019), Cs_xWO_3 (Li et al., 2018; Shi et al., 2018; Zeng et al., 2015), $Cu_{2-x}S$ (Shao et al., 2020; Sun et al., 2017; Zhou et al., 2019), $Cu_{2-x}Se$ (Liu et al., 2019; Xie et al., 2019; Zhang et al., 2018) and $Cu_{2-x}Te$ (Srathongluan et al., 2015; Yang et al., 2013; Zheng et al., 2016). Note that the existence of abundant intrinsic vacancies produces a large number of free carriers within nonstoichiometric semiconductors, which induces LSPR in the NIR region. Different from LSPR of plasmonic metal nanostructures, which is due to the coherent oscillation of conduction electrons, LSPR of nonstoichiometric semiconductors is because of the intrinsic vacancies associated with nonstoichiometry, which induces formation of free carriers. For instance, Cu vacancies of $Cu_{2-x}S$ can cause formation of plentiful holes. On the other hand, oxygen vacancies of WO_{3-x} generate abundant electrons. By adjusting the nonstoichiometry, i.e. the x value, the intensity and frequency of LSPR of these nonstoichiometric semiconductors can be controlled, providing an alternative approach to utilizing the NIR spectrum.

Cs_xWO_3 (CWO) is a nonstoichiometric semiconductor having large bandgap energy of 3.0 eV. The mixed valence of W^{5+} and W^{6+} in CWO produces abundant oxygen vacancies, resulting in the appearance of LSPR in the NIR region. This peculiar optical feature evokes the interest to develop full spectrum-driven photocatalytic systems based on the use of CWO. Li et al. combined the LSPR feature of CWO with the visible light responsive CdS to create a Z-scheme heterostructure photocatalyst (CSCWO) that can be driven by full solar spectrum (Li et al., 2020b). Fig. 9(a) displays the absorption spectra of CSCWO with different CWO ratios. Noticeably, all of the CSCWO samples showed multiple, broad absorption bands across the UV, visible to NIR region.

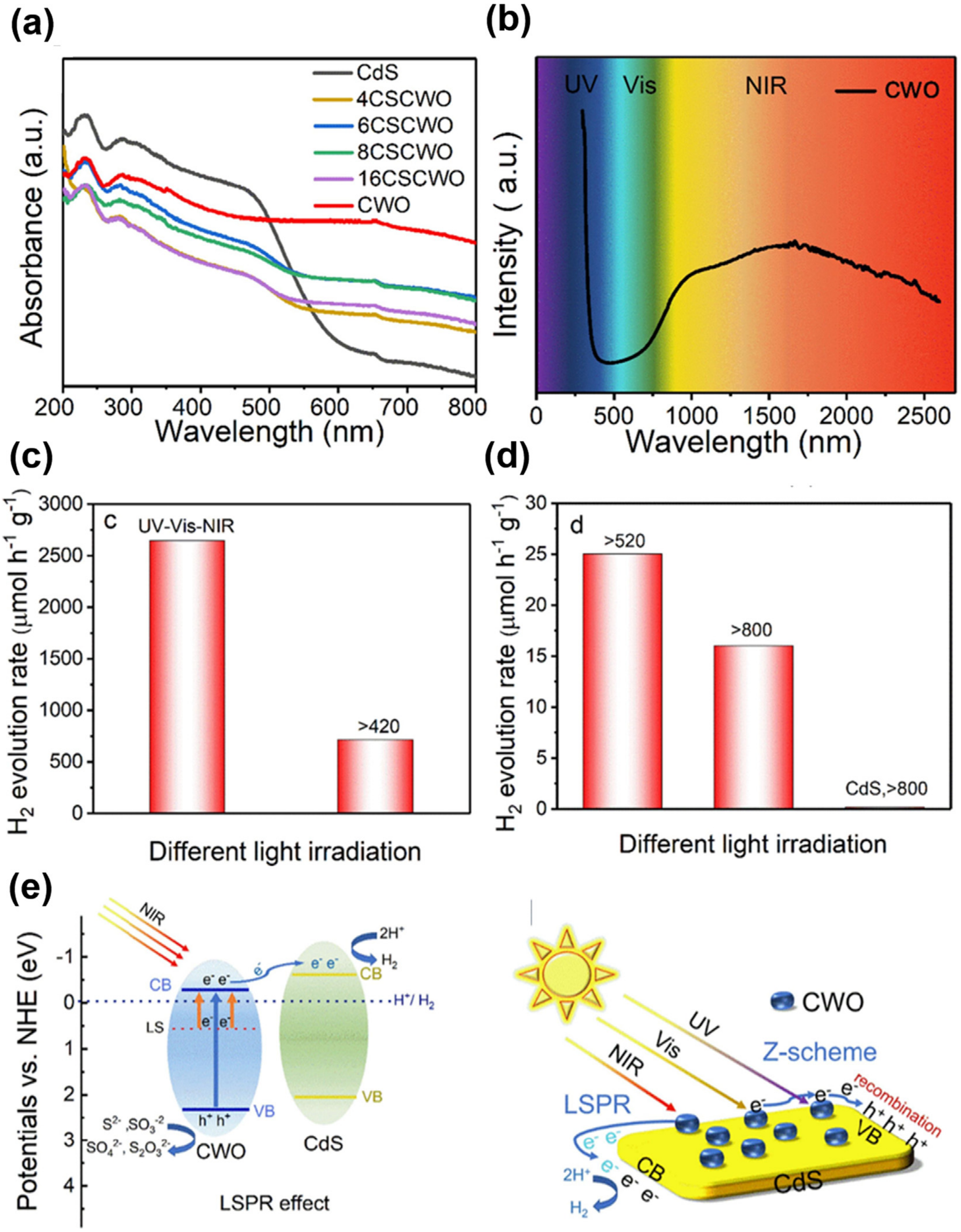

Fig. 9 (a) Diffuse reflectance spectra of CSCWO with different CWO ratios. (b) Absorption spectrum of CWO. (c-d) Photocatalytic hydrogen production on CSCWO under different illumination conditions. (e) Plausible charge transfer mechanism for CSCWO. Reprinted with permission (Li et al., 2020b). Copyright 2020, Elsevier.

The absorption at UV and visible resulted from the bandgap transition of CWO and CdS. The absorption behind 520 nm can be assigned to the LSPR of CWO. The pronounced LSPR absorption of CWO can be further identified from Fig. 9(b), which exhibited an unambiguous absorption band extended to 2500 nm. To estimate the LSPR-enhanced photoactivity, the samples were tested for hydrogen production under different illumination conditions. As Fig. 9(c) and 9(d) show, the CSCWO exhibited full spectrum-driven photoactivity toward hydrogen production. Even though the photoactivity of CSCWO mainly came from the illumination at $\lambda < 520$ nm, the CSCWO still showed noticeable photoactivity under illumination at $\lambda > 800$ nm, a region where pure CdS was inactive. This observation suggested that the introduced CWO rendered CdS NIR photoactivity by exploiting the peculiar LSPR. In Fig. 9(e), the charge transfer scenario of CSCWO was proposed. The band structure of CdS and CWO ensured effective photons harvesting from UV to visible regions. The LSPR of CWO enabled CSCWO to utilize the NIR photons, achieving full spectrum responsive photoactivity. With the support of Z-scheme mechanism, CSCWO exhibited outstanding photoactivity for hydrogen evolution.

Lian et al. also devised an LSPR-induced NIR-driven photocatalyst model composed of CdS/Cu_7S_4 p-n heterostructures, which demonstrated an unprecedented quantum efficiency (Lian et al., 2019). In this work, CdS/Cu_7S_4 heterodimers were synthesized by performing partial cation exchange on Cu_7S_4 with Cd^{2+}. Fig. 10(a_1-a_2) shows TEM images for the starting Cu_7S_4 and the resulting CdS/Cu_7S_4. The photocatalytic activity of hydrogen production was measured under NIR illumination (λ > 800 nm). In Fig. 10 (b), pure Cu_7S_4 and physical mixture of Cu_7S_4 and CdS did not produce hydrogen; only CdS/Cu_7S_4 showed photoactivity. The results implied that the LSPR-induced hot electron injection from Cu_7S_4 to CdS played a significant role in water splitting reaction. In Fig. 10 (c), the apparent quantum yield (AQY) of hydrogen production can reach as high as 3.8% at 1100 nm for CdS/Cu_7S_4. The samples still showed vigorous photoactivity even under illumination at 2400 nm. Importantly, the recorded quantum efficiency at different illumination wavelengths was spectrally consistent with the corresponding LSPR absorption spectrum. This outcome confirmed that the NIR photoactivity of CdS/Cu_7S_4 indeed originated from the LSPR excitation of Cu_7S_4. The concept of LSPR-induced hot electron transfer at the p-n junction provides an intelligent approach for the rational design of NIR-driven semiconductor photoelectrodes.

3. Outlook and perspectives

Table 1 summarizes the recent developments on NIR-responsive photoelectrodes and photocatalysts. Although the efficiency of PEC cells is far from the target, PEC water splitting is still considered a hopeful approach of converting solar power into renewable hydrogen fuels. How to improve the effectiveness of PEC systems has been extensively studied. There are many vital factors deeply affecting the efficiency, which include photons harvesting, charge transfer, charge separation and charge injection at the surface. Among these factors, photons harvesting ability is the most decisive one because it directly determines the theoretical STH efficiency. Chalcogenides and chalcopyrites semiconductors are ideal candidates as photons harvesting elements by virtue of their narrow bandgap. However, severe photocorrosion is commonly observed in these semiconductors, especially when Cu, S, or Se moieties are present. Although many delicate surface protection methods have been proposed, the exact role of protec-

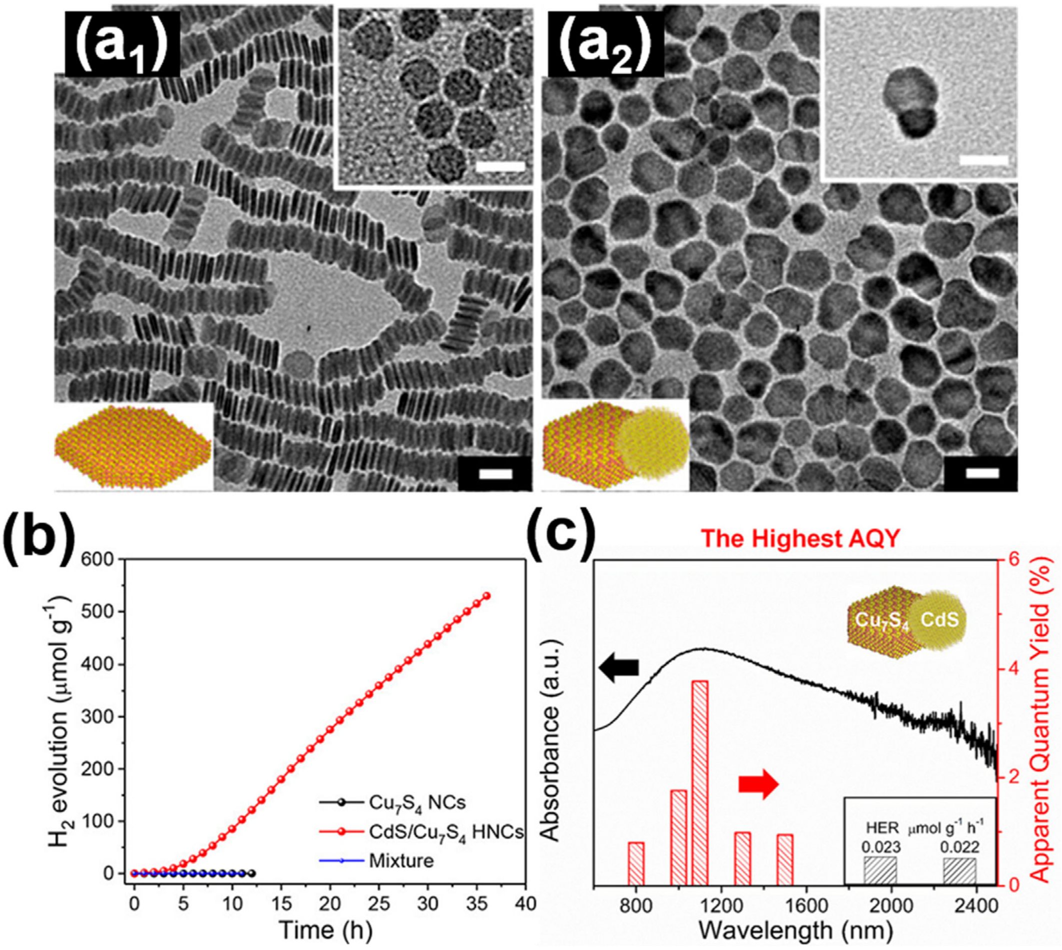

Fig. 10 TEM images for (a_1) starting Cu_7S_4, (a_2) resulting CdS/Cu_7S_4. (b) Hydrogen production on pure Cu_7S_4 and CdS/Cu_7S_4 under NIR illumination. (c) Quantum efficiency and the corresponding LSPR absorption spectrum for CdS/Cu_7S_4. Reprinted with permission (Lian et al., 2019). Copyright 2019, American Chemical Society.

Table 1 Summary of recent developments on NIR-responsive photoelectrodes and photocatalysts.

Chalcogenides

Photoelectrodes	Electrolyte	Light Source	Photocurrent	Efficiency at NIR	Reference
SnS	0.1 M $Eu(NO_3)_3$	AM 1.5G, 100 mW/cm^2	0.17 mA/cm^2 (−0.7 V vs. SCE)	–	Antunez et al., 2014
Sb-doped SnS	0.1 M $Na_2S_2O_3$	While light ($\lambda > 400$ nm), 410 mW/cm^2	0.32 mA/cm^2 (0.36 V vs. RHE)	–	Seal et al., 2015
SnS/CdS	0.5 M H_2SO_4	AM 1.5G,100 mW/cm^2	0.015 mA/cm^2 (0 V vs. RHE)	–	Gao et al., 2016
SnS	0.24 M Na_2S/0.34 M Na_2SO_3	AM 1.5G, 100 mW/c m^2	0.08 mA/cm^2	AQY = 0.31% (with UV cut-off filter)	Shiga et al., 2016
SnS/CdS/TiO_2	0.5 M H_2SO_4	AM 1.5G with 500 nm cut-off filter, 80 mW/cm^2	2.4 mA/cm^2 (0 V vs. RHE)	IPCE = 4.4% (λ = 900 nm, 0 V vs. RHE)	Cheng et al., 2018
SnS	0.1 M HCl	AM 1.5G, 100 mW/cm^2	5.6 mA/cm^2 (0.3 V vs. RHE)	IPCE = 1.9% (λ = 750 nm, −0.3 V vs. RHE)	Patel et al., 2017
Sb_2Se_3/MoS_x/S	1 M H_2SO_4	AM 1.5G, 100 mW/cm^2	14.0 mA/cm^2 (0 V vs. RHE)	IPCE = 7.5% (λ = 1000 nm, 0 V vs. RHE)	Prabhakar et al., 2017
Sb_2Se_3/TiO_2/Pt	0.5 M H_2SO_4	AM 1.5G, 100 mW/cm^2	4.5 mA/cm^2 (−0.2 V vs. RHE)	–	Kim et al., 2017
Sb_2Se_3/CdSe/TiO_2/Pt	0.5 M Na_2SO_4 buffered with 0.25 M Na_2HPO_4/0.25 M NaH_2PO_4	AM 1.5G, 100 mW/cm^2	8.6 mA/cm^2 (0 V vs. RHE)	IPCE = 2.5% (λ = 1000 nm, 0 V vs. RHE)	Zhang et al., 2017
Sb_2Se_3/TiO_2/Pt	0.1 M H_2SO_4	AM 1.5G, 100 mW/cm^2	12.5 mA/cm^2 (0 V vs. RHE)	IPCE = 3.5% (λ = 950 nm, 0 V vs. RHE)	Yang et al., 2018
Sb_2Se_3/TiO_2/Pt	H_2SO_4 (pH = 1)	AM 1.5G, 100 mW/cm^2	13.6 mA/cm^2 (0 V vs. RHE)	IPCE = 26% (λ = 800 nm, 0 V vs. RHE)	Park et al., 2019
Cu:NiO/Sb_2Se_3/TiO_2/Pt	H_2SO_4 (pH = 1)	AM 1.5G, 100 mW/cm^2	17.5 mA/cm^2 (0 V vs. RHE)	IPCE = 29% (λ = 900 nm, 0 V vs. RHE)	Lee et al., 2019b
Sb_2Se_3/TiO_2/Pt	H_2SO_4 (pH = 1)	AM 1.5G, 100 mW/cm^2	30.0 mA/cm^2 (0 V vs. RHE)	IPCE = 62% (λ = 800 nm, 0 V vs. RHE)	Park et al., 2020
WSe_2/Pt-Cu	1 M H_2SO_4	AM 1.5G,100 mW/cm^2	4.0 mA/cm^2(0 V vs. RHE)	IPCE = 5% (λ = 800 nm, 0 V vs. RHE)	Yu et al., 2018

Chalcopyrites

Photoelectrodes	Electrolyte	Light Source	Photocurrent	Efficiency at NIR	Reference
$CuInS_2$/CdS/AZO/TiO_2/Pt	0.5 M Na_2SO_4/0.1 M KH_2PO_4	AM 1.5G,100 mW/cm^2	3.5 mA/cm^2(−0.3 V vs. RHE)	IPCE = 7.4% (λ = 800 nm, 0 V vs. RHE)	Luo et al., 2015
Cu(In,Ga)S_2/CdS/Pt	0.1 M Na_2SO_4	AM 1.5G, 100 mW/cm^2	6.8 mA/cm^2 (0 V vs. RHE)	IPCE = 8% (λ = 800 nm, 0 V vs. RHE)	Septina et al., 2015

Plasmonic metals and semiconductors

Photoelectrodes/photocatalysts	Electrolyte	Light source	Photocurrent/hydrogen production	Efficiency at NIR	Reference
Al/NiO_x/Au	0.5 M Na_2SO_4	AM 1.5G, 100 mW/cm^2	0.025 mA/cm^2 (0 V vs. RHE)	IPCE = 0.055% (λ = 875 nm, 0 V vs. RHE)	Robatjazi et al., 2015
TiO_2/Au	1 M NaOH	AM 1.5G, 100 mW/cm^2	1.49 mA/cm^2 (1.01 V vs. RHE)	IPCE = 0.015% (λ = 750 nm, 0 V vs. Ag/AgCl)	Pu et al., 2013
TiO_2/Au	0.5 M Na_2SO_4Methanol (30 vol	Xe Lamp, 300 W	0.125 mA/cm^2	IPCE = 0.25% (λ = 800 nm)	Zhang et al., 2016

(*continued on next page*)

Table 1 *(continued)*

Photoelectrodes/ photocatalysts	Electrolyte	Light source	Photocurrent/hydrogen production	Efficiency at NIR	Reference
Plasmonic metals and semiconductors					
	%)		15 mL/mg$_{Au}$/h (λ > 420nm)		
$WO_{3-x}/TiO_2/Pt$	Methanol (30 vol%)	Xe Lamp, 300 W	17.7 mmol/g/h	–	Pan et al., 2017
a-WO_{3-x}/Ag	0.5 M Na_2SO_4	AM 1.5G,100 mW/cm^2	0.027 mA/cm^2(1.4 V vs. RHE)	IPCE = 6.1%(λ = 650 nm, 1.4 V vs. RHE)	Ren et al., 2019
g-$C_3N_4/WO_{3-x}/Pt$	Triethylamine (10 vol%)	λ = 365~940 nm,100.1 mW/cm^2	3.361 mmol/g/h	10 μmol/g/h(λ = 980 nm)	Shi et al., 2018
$Cu_{2-x}Se$/rGO	0.35 M Na_2S/0.15 M Na_2SO_3	Xe lamp, 300W	3.123 mmol/g/h	–	Xie et al., 2019
$Cs_{0.33}WO_3/CdS$	Na_2S/Na_2SO_3	Visible Light(λ > 420 nm)	2.648 mmol/g/h	16 μmol/g/h (λ > 800 nm)	Li et al., 2020b
$Cu_7S_4/CdS/Pt$	0.25 M Na_2S/0.35 M Na_2SO_3	NIR Light(λ > 800 nm)	16 μmol/g/h	AQY = 3.8% (λ = 1100 nm)	Lian et al., 2019

tive layers is equivocal, giving rise to inconsistent results even under similar experimental conditions. Developing a generalized approach to addressing the instability issues of chalcogenides and chalcopyrites photoelectrodes is therefore imperative. Additionally, these narrow-bandgap semiconductors sacrifice their chemical potential in order to absorb more incident photons. This feature inevitably reduces the thermodynamics driving force of water splitting to deteriorate the PEC performance.

Plasmonic metal nanostructures with specific size and shape are capable of harvesting low-energy photons by LSPR, which can be employed to sensitize semiconductor photoelectrodes to NIR region. Despite enormous progress made to promote the evolution of this metal-sensitized semiconductor system, there are still many conspicuous challenges. First, the mechanism of LSPR-induced photoactivity is controversial. Not only near-field effect can participate in PEC reactions, but far-field factor can also be prevalent during charge transfer and recombination processes. This complexity would entangle the mechanistic comprehension on the fundamental principle of plasmonic metal-sensitized photoelectrodes. Last but not the least, the LSPR-induced photoactivity enhancement has been mediocre, usually < 1%. The ultrafast recombination dynamics of hot carriers makes it difficult to steer plasmonic metal nanostructures in PEC water splitting. Besides plasmonic metals, nonstoichiometric semiconductors also exhibit LSPR absorption that can be exploited to create NIR-driven PEC systems. Relative to plasmonic metals, employment of nonstoichiometric semiconductors as NIR-driven photoelectrodes is still in its infancy, requiring continuous effort to make significant breakthrough. In summary, the exploration of NIR-driven photoelectrodes is of great importance yet immature. There is still substantial room for performance improvement and property optimization in order for the widespread deployment of PEC technology.

Declaration of Competing Interest

The author declare that there is no conflict of interest.

Acknowledgements

This work was financially supported by the Ministry of Science and Technology (MOST) of Taiwan under grants MOST 107-2113-M-009-004, MOST 108-2628-M-009-004-MY3 and MOST 108-2218-E-009-039-MY3, and the Japan Society for the Promotion of Science (JSPS) with KAKENHI Grant # 18K14085. Y.-J. Hsu also acknowledges the budget support from the Center for Emergent Functional Matter Science of National Chiao Tung University from The Featured Areas Research Center Program within the framework of the Higher Education Sprout Project by the Ministry of Education in Taiwan.

References

Antunez, P.D., Torelli, D.A., Yang, F., Rabuffetti, F., Lewis, N.S., Brutchey, R.L., 2014. Low temperature solution-phase deposition of SnS thin films 5444–2446 Chem. Mater. 26 (19). https://doi.org/10.1021/cm503124u.

Asunción-Nadal, V.D.L., Jurado-Sánchez, B., Vázquez, L., Escarpa, A., 2020. Near infrared-light responsive WS_2 microengines with high-performance electro- and photo-catalytic activities. Chem. Sci. 11 (1), 132–140. https://doi.org/10.1039/C9SC03156A.

Atkin, P., Daeneke, T., Wang, Y., Carey, B.J., Berean, K.J., Clark, R.M., Ou, J.Z., Trinchi, A., Cole, I.S., Kalantar-zadeh, K., 2016. 2D WS_2/carbon dot hybrids with enhanced photocatalytic activity. J. Mater. Chem. A 4 (35), 13563–13571. https://doi.org/10.1039/C6TA06415A.

Bagal, I.V., Chodankar, N.R., Hassan, M.A., Waseem, A., Johar, M.A., Kim, D.-H., Ryu, S.-W., 2019. Cu_2O as an emerging photocathode for solar water splitting – A status review. Int. J. Hydrog. Energy 44 (39), 21351–21378. https://doi.org/10.1016/j.ijhydene.2019.06.184.

Bai, H., Yi, W., Li, J., Xi, G., Li, Y., Yanga, H., Liu, J., 2015. Direct growth of defect-rich MoO_{3-x} ultrathin nanobelts for efficiently catalyzed conversion of isopropyl alcohol to propylene under visible light. J. Mater. Chem. A 4 (5), 1566–1571. https://doi.org/10.1039/C5TA08603E.

Birant, G., Wild, J.D., Meuris, M., Poortmans, J., Vermang, B., 2019. Dielectric-based rear surface passivation approaches for Cu(In, Ga) S_e2 solar cells- a review. Appl. Sci. 9 (4), 677. https://doi.org/10.3390/app9040677.

Chen, C.-W., Tsai, H.-W., Wang, Y.-C., Shih, Y.-C., Su, T.-T., Yang, C.-H., Lin, W.-S., Shen, C.-H., Shieh, J.-M., Chueh, Y.-L., 2019. Rear-passivated ultrathin Cu(In, Ga)S_e2 films by A_l2_O3 nanostructures using glancing angle deposition toward photovoltaic devices with enhanced efficiency. Adv. Funct. Mater. 29 (48), 1905040. https://doi.org/10.1002/adfm.201905040.

Cheng, W., Singh, N., Elliott, W., Lee, J., Rassoolkhani, A., Jin, X., McFarland, E.W., Mubeen, S., 2018. Earth-abundant tin sulfide-based photocathodes for solar hydrogen production. Adv. Sci. 5 (1), 1700362. https://doi.org/10.1002/advs.201700362.

Archer, D., 2011. Global Warming: Understanding the Forecast, Wiley-VCH Verlag GmbH & Co. KGaA, Weinheim, Second Edition.

Do, H.H., Nguyen, D.L.T., Nguyen, X.C., Le, T.-H., Nguyen, T.P., Trinh, Q.T., Ahn, S.H., Vo, D.-V., Kim, S.Y., Le, Q.V., 2020. Recent progress in TiO2-based photocatalysts for hydrogen evolution reaction: a review. Arab. J. Chem. 13 (2), 3653–3671. https://doi.org/10.1016/j.arabjc.2019.12.012.

Efekhari, A., 2017. Molybdenum diselenide ($MoSe_2$) for energy storage, catalysis, and optoelectronics. Appl. Mater. Today 8, 1–17. https://doi.org/10.1016/j.apmt.2017.01.006.

Gao, W., Wu, C., Cao, M., Huang, J., Wang, L., Shen, Y., 2016. Thickness tunable SnS nanosheets for photoelectrochemical water splitting. J. Alloys Compd. 688, 668–674. https://doi.org/10.1016/j.jallcom.2016.07.083.

Grätzel, M., 2001. Photoelectrochemical cells. Nature 414 (15), 338–344. https://doi.org/10.1038/35104607.

Guo, W., Le, Q.V., Do, H.H., Hasani, A., Tekalgne, M., Bae, S.-R., Lee, T.H., Jang, H.W., Ahn, S.H., Kim, S.Y., 2019. Ni_3S_4@$MoSe_2$ composites for hydrogen evolution reaction. Appl. Sci. 9 (23), 5035. https://doi.org/10.3390/app9235035.

Hasani, A., Tekalgne, M., Le, Q.V., Jang, H.W., Kim, S.Y., 2019a. Two-dimensional materials as catalysts for solar fuels: hydrogen evolution reaction and CO_2 reduction. J. Mater. Chem. A 7 (2), 430–454. https://doi.org/10.1039/C8TA09496A.

Hasani, A., Le, Q.V., Tekalgne, M., Choi, M.-J., Choi, S., Lee, T.H., Kim, H., Ahn, S.H., Jang, H.W., Kim, S.Y., 2019b. Fabrication of a WS_2/p-Si heterostructure photocathode using direct hybrid thermolysis. ACS Appl. Mater. Interfaces 11 (33), 29910–29916. https://doi.org/10.1021/acsami.9b08654.

Hasani, A., Le, Q.V., Tekalgne, M., Choi, M.-J., Lee, T.H., Jang, H.W., Kim, S.Y., 2019c. Direct synthesis of two-dimensional MoS_2 on p-type Si and application to solar hydrogen production. NPG Asia Mater. 11, 47. https://doi.org/10.1038/s41427-019-0145-7.

Hou, W., Cronin, S.B., 2013. A review of surface plasmon resonance-enhanced photocatalysis. Adv. Funct. Mater. 23 (13), 1612–1619. https://doi.org/10.1002/adfm.201202148.

Ishizuka, S., 2019. $CuGaSe_2$ thin film solar cells: challenges for developing highly efficient wide-gap chalcopyrite photovoltaics. Phys. Status Solidi A 216 (15), 1800873. https://doi.org/10.1002/pssa.201800873.

Jiang, C., Moniz, S.J.A., Wang, A., Zhang, T., Tang, J., 2017. Photoelectrochemical devices for solar water splitting – materials and challenges. Chem. Soc. Rev. 46 (15), 4645–4660. https://doi.org/10.1039/C6CS00306K.

Jin, H., Guo, C., Liu, X., Liu, J., Vasileff, A., Jiao, Yan, Zheng, Y., Qiao, S.-Z., 2018. Emerging two-dimensional nanomaterials for electrocatalysis. Chem. Rev. 118 (13), 6337–6408. https://doi.org/10.1021/acs.chemrev.7b00689.

Kasani, S., Zheng, P., Bright, J., Wu, N., 2019. Tunable visible-light surface plasmon resonance of molybdenum oxide thin films fabricated by E–beam evaporation. ACS Appl. Electron. Mater. 1 (11), 2389–2395. https://doi.org/10.1021/acsaelm.9b00555.

Kim, J.H., Hansora, D., Sharma, P., Jang, J.-W., Lee, J.S., 2019. Toward practical solar hydrogen production – an artificial photosynthetic leaf-to-farm challenge. Chem. Soc. Rev. 48 (7), 1908–1971. https://doi.org/10.1039/C8CS00699G.

Kim, J.H., Lee, J.S., 2019. Elaborately modified $BiVO_4$ photoanodes for solar water splitting. Adv. Mater. 31 (20), 1806938. https://doi.org/10.1002/adma.201806938.

Kim, J., Yang, W., Oh, Y., Lee, H., Lee, S., Shin, H., Kim, J., Moon, J., 2017. Self-oriented Sb_2Se_3 nanoedle photocathodes for water splitting obtained by a simple spin-coating method. J. Mater. Chem. A 5 (5), 2180–2187. https://doi.org/10.1039/C6TA09602F.

Lee, D.K., Lee, D., Lumley, M.A., Choi, K.-S., 2019a. Progress on ternary oxide-based photoanodes for use in photoelectrochemical cells for solar water splitting. Chem. Soc. Rev. 48 (7), 2126–2157. https://doi.org/10.1039/C8CS00761F.

Lee, H., Yang, W., Tan, J., Oh, Y., Park, J., Moon, J., 2019b. Cu-doped NiO_x as an effective hole-selective layer for a high-performance Sb_2Se_3 photocathode for photoelectrochemical water splitting. ACS Energy Lett. 4 (5), 995–1003. https://doi.org/10.1021/acsenergylett.9b00414.

Lee, H., Deshmukh, S., Wen, J., Costa, V.Z., Schuder, J.S., Sanchez, M., Ichimura, A.S., Pop, E., Wang, B., Newaz, A.K.M., 2019c. Layer-dependent interfacial transport and optoelectrical properties of MoS_2 on ultraflat metals. ACS Appl. Mater. Interfaces 11 (34), 31543–31550. https://doi.org/10.1021/acsami.9b09868.

Li, Y., Wu, X., Li, J., Wang, K., Zhang, G., 2018. Z-scheme g-C_3-N_4@Cs_xWO_3 heterostructure as smart window coating for UV isolating, Vis penetrating, NIR shielding and full spectrum photocatalytic decomposing VOCs. Appl. Catal. B 229, 218–226. https://doi.org/10.1016/j.apcatb.2018.02.024.

Li, Z., Zheng, M., Wei, N., Lin, Y., Chu, W., Xu, R., Wang, H., Tian, J., Cui, H., 2020a. Broadband-absorbing WO_{3-x} nanorod-decorated wood evaporator for highly efficient solar-driven interfacial steam generation. Sol. Energy Mater Sol. Cells 205,. https://doi.org/10.1016/j.solmat.2019.110254 110254.

Li, N., Fanb, H., Daib, Y., Kongb, J., Ge, L., 2020b. Insight into the solar utilization of a novel Z-scheme $Cs_{0.33}WO_3$/CdS heterostructure for UV–Vis-NIR driven photocatalytic hydrogen evolution. Appl. Surf. Sci. 508,. https://doi.org/10.1016/j.apsusc.2019.145200 145200.

Lian, Z., Sakamoto, M., Vequizo, J.J.M., Kumara Ranasinghe, C.S., Yamakata, A., Nagai, T., Kimoto, K., Kobayashi, Y., Tamai, N., Teranishi, T., 2019. Plasmonic p−n junction for infrared light to chemical energy conversion. J. Am. Chem. Soc. 141 (6), 2446–2450. https://doi.org/10.1021/jacs.8b11544.

Liu, Y., Shen, S., Zhang, J., Zhong, W., Huang, X., 2019. $Cu_{2-x}Se$/CdS composite photocatalyst with enhanced visible light photocatalysis activity. Appl. Surf. Sci. 478, 762–769. https://doi.org/10.1016/j.apsusc.2019.02.010.

Lopes, T.S., Cunha, J.M.V., Bose, S., Barbosa, J.R.S., Borme, J., Donzel-Gargand, O., Rocha, C., Silva, R., Hultqvist, A., Chen, W.-C., Silva, A.G., Edoff, M., Fernandes, P.A., Salomé, M.P.,

2019. Rear optical reflection and passivation using a nanopatterned metal/dielectric structure in thin-film solar cells. IEEE J. Photovolt. 9 (5), 1421–1427. https://doi.org/10.1109/JPHOTOV.2019.2922323.

Luo, J., Tilley, S.D., Steier, L., Schreier, M., Mayer, M.T., Fan, H.J., Grätzel, M., 2015. Solution transformation of Cu_2O into $CuInS_2$ for solar water splitting. Nano Lett. 15 (2), 1395–1402. https://doi.org/10.1021/nl504746b.

Ma, W., Yao, B., Zhang, W., He, Y., Yu, Y., Niu, J., Wang, C., 2018. A novel multi-flaw MoS_2 nanosheet piezocatalyst with superhigh degradation efficiency for ciprofloxacin. Environ. Sci.: Nano 5 (12), 2876–2887. https://doi.org/10.1039/C8EN00944A.

Nguyen, T.P., Le, Q.V., Choi, S., Lee, T.H., Hong, S.-P., Choi, K.S., Jang, H.W., Lee, M.H., Park, T.J., Kim, S.Y., 2018. Surface extension of MeS_2 (Me = Mo or W) nanosheets by embedding MeS_x for hydrogen evolution reaction. Electrochim. Acta 292, 136–141. https://doi.org/10.1016/j.electacta.2018.08.115.

Nguyen, V.-H., Nguyen, T.P., Le, T.-H., Vo, D.-V., Nguyen, D.L., Trinh, Q.T., Kim, I.T., Le, Q.V., 2020a. Recent advances in two-dimensional transition metal dichalcogenides as photoelectrocatalyst for hydrogen evolution reaction. J. Chem. Technol. Biotechnol. https://doi.org/10.1002/jctb.6335.

Nguyen, V.-H., Nguyen, B.-S., Hu, C., Nguyen, C.C., Nguyen, D.L. T., Kinh, M.T.N., Vo, D.-V.N., Trinh, Q.T., Shokouhimehr, M., Hasani, A., Kim, S.Y., Le, Q.V., 2020b. Novel architecture titanium carbide ($Ti_3C_2T_x$) MXene cocatalysts toward photocatalytic hydrogen production: a mini-review. Nanomaterials 10 (4), 602. https://doi.org/10.3390/nano10040602.

Nguyen, T.P., Nguyen, D.L.T., Nguyen, V.-H., Le, T.-H., Ly, Q.V., Vo, D.-V.N., Nguyen, Q.V., Le, H.S., Jang, H.W., Kim, S.Y., Le, Q.V., 2020c. Facile synthesis of WS_2 hollow spheres and their hydrogen evolution reaction performance. Appl. Surf. Sci. 505,. https://doi.org/10.1016/j.apsusc.2019.144574 144574.

Nguyen, T.P., Kim, S.Y., Lee, T.H., Jang, H.W., Le, Q.V., Kim, I.T., 2020d. Facile synthesis of $W_2C@WS_2$ alloy nanoflowers and their hydrogen generation performance. Appl. Surf. Sci. 504,. https://doi.org/10.1016/j.apsusc.2019.144389 144389.

Nguyen, T.P., Nguyen, D.M.T., Tran, D.L., Le, H.K., Vo, D.-V.N., Lam, S.S., Varma, R.S., Shokouhimehr, M., Nguyen, C.C., Le, Q. V., 2020e. MXenes: applications in electrocatalytic, photocatalytic hydrogen evolution reaction and CO_2 reduction. Mol. Catal. 486,. https://doi.org/10.1016/j.mcat.2020.110850 110850.

Odda, A.H., Xu, Y., Lin, J., Wang, G., Ullah, N., Zeb, A., Liang, K., Wen, L.-P., Xu, A.-W., 2019. Plasmonic MoO_{3-x} nanoparticles incorporated in Prussian blue frameworks exhibit highly efficient dual photothermal/photodynamic therapy. J. Mater. Chem. B 7 (12), 2032–2042. https://doi.org/10.1039/C8TB03148G.

Pan, L., Kim, J.H., Mayer, M.T., Son, M.-K., Ummadisingu, A., Lee, J.S., Hagfeldt, A., Luo, J., Grätzel, M., 2018. Boosting the performance of Cu_2O photocathodes for unassisted solar water splitting devices. Nat. Catal. 1 (15), 412–420. https://doi.org/10.1038/s41929-018-0077-6.

Pan, L., Zhang, J., Jia, X., Ma, Y.-H., Zhang, X., Wang, L., Zou, J.-J., 2017. Highly efficient Z-scheme WO_{3-x} quantum dots/TiO_2 for photocatalytic hydrogen generation Chinese. J. Catal. 38 (2), 253–259. https://doi.org/10.1016/S1872-2067(16)62576-7.

Park, J., Yang, W., Oh, Y., Tan, J., Lee, H., Boppella, R., Moon, J., 2019. Efficient solar-to-hydrogen conversion from neutral electrolytes using morphology-controlled Sb_2Se_3 light absorbers. ACS Energy Lett. 4 (2), 517–526. https://doi.org/10.1021/acsenergylett.8b02323.

Park, J., Yang, W., Tan, J., Lee, H., Yun, J.W., Shim, S.G., Park, Y. S., Moon, J., 2020. Hierarchal nanorod-derived bilayer strategy to enhance the photocurrent density of Sb_2Se_3 photocathodes for photoelectrochemical water splitting. ACS Energy Lett. 5 (1), 136–145. https://doi.org/10.1021/acsenergylett.9b02486.

Patel, M., Kumar, M., Kim, J., Kim, Y.K., 2017. Photocurrent enhancement by a rapid thermal treatment of nanodish-shaped SnS photocathodes. J. Phys. Chem. Lett. 8 (24), 6099–6105. https://doi.org/10.1021/acs.jpclett.7b02998.

Prabhakar, R.R., Septina, W., Siol, S., Moehl, T., Wick-Joliat, R., Tilley, S.D., 2017. Photocorrosion-resistant Sb_2Se_3 photocathodes with earth abundant MoS_x hydrogen evolution catalyst. J. Mater. Chem. A 5 (44), 23139–23145. https://doi.org/10.1039/C7TA08993G.

Pu, Y.-C., Wang, G., Chang, K.-D., Ling, Y., Lin, Y.-K., Fitzmorris, B.C., Liu, C.-M., Lu, X., Tong, Y., Zhang, J.Z., Hsu, Y.-J., Li, Y., 2013. Au nanostructure-decorated TiO_2 nanowires exhibiting photoactivity across entire UV-visible region for photoelectrochemical water splitting. Nano Lett. 13 (8), 3817–3823. https://doi.org/10.1021/nl4018385.

Ren, Y., Li, C., Xu, Q., Yan, J., Li, Y., Yuan, P., Xia, H., Niu, C., Yang, X., Jia, Y., 2019. Two-dimensional amorphous heterostructures of Ag/a-WO_{3-x} for highefficiency photocatalytic performance. Appl. Catal. B 245, 648–655. https://doi.org/10.1016/j.apcatb.2019.01.015.

Robatjazi, H., Bahauddin, S.M., Doiron, C., Thomann, I., 2015. Direct plasmon-driven photoelectrocatalysis. Nano Lett. 15 (9), 6155–6161. https://doi.org/10.1021/acs.nanolett.5b02453.

Seal, M., Singh, N., McFarland, E.W., Baltrusaitis, J., 2015. Electrochemically deposited Sb and In doped tin sulphide (SnS) photoelectrodes. J. Phys. Chem. C 119 (12), 6471–6480. https://doi.org/10.1021/jp512927y.

Septina, W., Gunawan, Ikeda, S., Harada, T., Higashi, M., Abe, R., Matsumura, M., 2015. Photosplitting of water from wide-gap Cu (In,Ga)S2 thin films modified with a CdS layer and Pt nanoparticles for a high-onset-potential photocathode. J. Phys. Chem. C 119(16), 8576-8583.

Shao, X., Zhang, T., Li, B., Wu, Y., Ma, X., Wang, J., Jiang, S., 2020. Cu-Deficient plasmonic $Cu_{2-x}S$ nanocrystals induced tunable photocatalytic activities. CrystEngComm 22 (4), 678–685. https://doi.org/10.1039/C9CE01501A.

Sharma, P., Jang, J.-W., Lee, J.S., 2019. Key strategies to advance the photoelectrochemical water splitting performance of α-Fe_2O_3 photoanode. ChemCatChem 11 (1), 157–179. https://doi.org/10.1002/cctc.201801187.

Shen, S., Lindley, S.A., Chen, X., Zhang, J.Z., 2016. Hematite heterostructures for photoelectrochemical water splitting: rational materials design and charge carrier dynamics. Energy Environ. Sci. 9, 2744–2775. https://doi.org/10.1039/C6EE01845A.

Shi, A., Li, H., Yin, S., Zhang, J., Wang, Y., 2018. H_2 evolution over g-C_3N_4/Cs_xWO_3 under NIR light. Appl. Catal. B 228, 75–86. https://doi.org/10.1016/j.apcatb.2018.01.070.

Shiga, Y., Umezawa, N., Srinivasan, N., Koyasu, S., Sakai, E., Miyauchi, M., A metal sulphide photocatalyst composed of ubiquitous elements for solar hydrogen production. Chem. Commun. 52(47), 7470–7473. https://doi.org/10.1039/C6CC03199D.

Sivula, K., Krol, R.V.D., 2016. Semiconducting materials for photoelectrochemical energy conversion. Nat. Rev. Mater. 1, 1–16. https://doi.org/10.1038/natrevmats.2015.10.

Srathongluan, P., Kuhamaneechot, R., Sukthao, P., Vailikhit, V., Choopun, S., Tubtimtae, A., 2015. Photovoltaic performances of $Cu_{2-x}Te$ sensitizer based on undoped and indium^{3+}-doped TiO_2 photoelectrodes and assembled counter electrodes. J. Colloid Interface Sci. 463, 222–228. https://doi.org/10.1016/j.jcis.2015.10.052.

Su, T., Hood, Z.D., Naguib, M., Bai, L., Luo, S., Rouleau, C.M., Ivanov, I.N., Ji, H., Qin, Z., Wu, Z., 2019. 2D/2D heterojunction of Ti_3C_2/g-C_3N_4 nanosheets for enhanced photocatalytic hydrogen evolution. Nanoscale 11 (17), 8138–8149. https://doi.org/10.1039/C9NR00168A.

Sun, S., Li, P., Liang, S., Yang, Z., 2017. Diversified copper sulfide ($Cu_{2-x}S$) micro-/nanostructures: a comprehensive review on synthesis, modifications and applications. Nanoscale 9 (32), 11357–11404. https://doi.org/10.1039/C7NR03828C.

Tayebi, M., Lee, B.-K., 2019. Recent advances in $BiVO_4$ semiconductor materials for hydrogen production using photoelectrochemical water splitting. Renew. Sust. Energ. Rev. 111, 332–343. https://doi.org/10.1016/j.rser.2019.05.030.

Tekalgne, M., Hasani, A., Le, Q.V., Kim, S.Y., 2019a. Transition metal dichalcogenide-based composites for hydrogen production. Funct. Compos. Struct. 1,. https://doi.org/10.1088/2631-6331/ab0c81 012001.

Tekalgne, M., Hasani, A., Le, Q.V., Nguyen, T.P., Choi, K.S., Lee, T. H., Jang, H.W., Luo, Z., Kim, S.Y., 2019b. CdSe quantum dots doped WS_2 nanoflowers for enhanced solar hydrogen production. Phys. Status. Solidi A 216 (9), 1800853. https://doi.org/10.1002/pssa.201800853.

Tekalgne, M.A., Hasani, A., Heo, D.Y., Le, Q.V., Nguyen, T.P., Lee, T.H., Ahn, S.H., Jang, H.W., Kim, S.Y., 2020a. SnO_2@WS_2/p-Si heterostructure photocathode for photoelectrochemical hydrogen production. J. Phys. Chem. C 124 (1), 647–652. https://doi.org/10.1021/acs.jpcc.9b09623.

Tekalgne, M.A., Nguyen, K.V., Nguyen, D.L., Nguyen, V.-H., Nguyen, T.P., Vo, D.-V.N., Trinh, Q.T., Hasani, A., Do, H.H., Lee, T.H., Jang, H.W., Le, H.S., Le, Q.V., Kim, S.Y., 2020b. Hierarchical molybdenum disulfide on carbon nanotube-reduced graphene oxide composite paper as efficient catalysts for hydrogen evolution reaction. J. Alloys Compd. 823,. https://doi.org/10.1016/j.jallcom.2020.153897 153897.

Tseng, C.-C., Wu, G., Chang, L.-B., Jeng, M.-J., Feng, W.-S., Chen, D.W., Chen, L.-C., Lee, K.-L., 2020. Effects of annealing on characteristics of $Cu_2ZnSnSe_4$/$CH_3NH_3PbI_3$/ZnS/IZO nanostructures for enhanced photovoltaic solar cells. Nanomaterials 10 (3), 521. https://doi.org/10.3390/nano10030521.

Unold, T., Kaufmann, C.A., 2012. Chalcopyrite thin-film materials and solar cells. Comprehensive Renewable energy, Elsevier, pp. 399–422.

Walter, M.G., Warren, E.L., McKone, J.R., Boettcher, S.W., Mi, Q., Santori, E.A., Lewis, N.S., 2010. Solar water splitting cells. Chem. Rev. 110 (11), 6446–6473. https://doi.org/10.1021/cr1002326.

Xie, X., Wang, R., Liu, E., Fan, J., Chen, B., Hu, X., 2019. Fabrication of a $Cu_{2-x}Se$/rGO heterojunction photocatalyst to achieve efficient photocatalytic H_2 generation. Int. J. Hydrog. Energy 44 (60), 32042–32053. https://doi.org/10.1016/j.ijhydene.2019.10.148.

Yang, H.-J., Chen, C.-Y., Yuan, F.-W., Tuan, H.-Y., 2013. Designed synthesis of solid and hollow $Cu_{2-x}Te$ nanocrystals with tunable near-infrared localized surface plasmon resonance. J. Phys. Chem. C 117 (42), 21955–21964. https://doi.org/10.1021/jp407559b.

Yang, S., Wang, Y., Sun, H., 2015. Advances and prospects for whispering gallery mode microcavities. Adv. Opt. Mater. 3 (9), 1136–1162. https://doi.org/10.1002/adom.201500232.

Yang, W., Ahn, J., Oh, Y., Tan, J., Lee, H., Park, J., Kwon, H.-C., Kim, J., Jo, W., Kim, J., Moon, J., 2018. Adjusting the anisotropy of 1D Sb_2Se_3 nanostructures for highly efficient photoelectrochemical water splitting. Adv. Energy Mater. 8 (14), 1702888. https://doi.org/10.1002/aenm.201702888.

Yang, W., Moon, J., 2019. Rapid advances in antimony triselenide photocathodes for solar hydrogen generation. J. Mater. Chem. A 7 (36), 20467–20477. https://doi.org/10.1039/C9TA07990D.

Ye, K.-H., Li, H., Huang, D., Xiao, S., Qiu, W., Li, M., Hu, Y., Mai, W., J., H., Yang, S., 2019. Enhancing photoelectrochemical water splitting by combing work function tuning and heterojunction engineering. Nat. Commun. 10 (15), 3687. https://doi.org/10.1038/s41467-019-11586-y.

Yu, X., Guijarro, N., Johnson, M., Sivula, K., 2018. Defect mitigation of solution-processed 2D WSe_2 nanoflakes for solar-to-hydrogen conversion. Nano Lett. 18 (1), 215–222. https://doi.org/10.1021/acs.nanolett.7b03948.

Yu, X., Sivula, K., 2016. Toward large-area solar energy conversion with semiconducting 2D transition metal dichalcogenides. ACS Energy Lett. 1 (1), 315–322. https://doi.org/10.1021/acsenergylett.6b00114.

Zeng, X., Zhou, Y., Ji, S., Luo, H., Yao, H., Huang, X., Jin, P., 2015. The preparation of a high performance nearinfrared shielding Cs_xWO_3/SiO_2 composite resin coating and research on its optical stability under ultraviolet illumination. J. Mater. Chem. C 3 (31), 8050–8060. https://doi.org/10.1039/C5TC01411E.

Zhang, J., Jin, X., Morales-Guzman, P.I., Yu, X., Liu, H., Zhang, H., Razzari, L., Claverie, J.P., 2016. Engineering the absorption and field enhancement properties of Au−TiO2 nanohybrids via whispering gallery mode resonances for photocatalytic water splitting. ACS Nano 10 (4), 4496–4503. https://doi.org/10.1021/acsnano.6b00263.

Zhang, L., Li, Y., Li, C., Chen, Q., Zhen, Z., Jiang, X., Zhong, M., Zhang, F., Zhu, H., 2017. Scalable low-band-gap Sb_2Se_3 thin-film photocathodes for efficient visible-near-infrared solar hydrogen evolution. ACS Nano 11 (12), 12753–12763. https://doi.org/10.1021/acsnano.7b07512.

Zhang, S., Huang, Q., Zhang, L., Zhang, H., Han, Y., Sun, Q., Cheng, Z., Qin, H., Dou, S., Li, Z., 2018. Vacancy engineering of $Cu_{2-x}Se$ nanoparticles with tunable LSPR and magnetism for dual-modal imaging guided photothermal therapy of cancer. Nanoscale 10 (7), 3130–3143. https://doi.org/10.1039/C7NR06937E.

Zheng, J., Dai, B., Liu, J., Liu, J., Ji, m., Liu, J., Zhou, Y., Xu, M., Zhang J., 2016. Hierarchical Self-Assembly of Cu7Te5 Nanorods into Superstructures with Enhanced SERS Performance. ACS Appl. Mater. Interfaces. 8 (51), 35426-35434. https://doi.org/10.1021/acsami.6b11058.

Zhou, L., Liu, Z., Guan, Z., Tian, B., Wang, L., Zhou, Y., Zhou, Y., Lei, J., Zhang, J., Liu, Y., 2019. 0D/2D plasmonic $Cu_{2-x}S$/g-C_3N_4 nanosheets harnessing UV-vis-NIR broad spectrum for photocatalytic degradation of antibiotic pollutant. Appl. Catal. B 263,. https://doi.org/10.1016/j.apcatb.2019.118326 118326.

Full Report, BP Statistical Review of World Energy 2019. https://www.bp.com/content/dam/bp/business-sites/en/global/corporate/pdfs/energy-economics/statistical-review/bp-stats-review-2019-full-report.pdf.